Suomi NPP VIIRS sensor data record verification, validation, and long-term performance monitoring

Changyong Cao,[1] Jack Xiong,[2] Slawomir Blonski,[3] Quanhua Liu,[3] Sirish Uprety,[4] Xi Shao,[3] Yan Bai,[5] and Fuzhong Weng[1]

[1]   The successful launch of the Suomi National Polar-orbiting Partnership Satellite on 28 October 2011 with the key instrument Visible Infrared Imaging Radiometer Suite signifies a new era of moderate-resolution imaging capabilities following the legacy of AVHRR and Moderate-Resolution Imaging Spectroradiometer (MODIS). After a year and half of calibration and validation, the Visible Infrared Imaging Radiometer Suite (VIIRS) instrument is performing very well. By early 2013, the sensor data records have achieved provisional maturity status and have been used in the routine production of more than 20 environmental data records by users worldwide. Based on comparisons with MODIS, the VIIRS reflective solar band radiometric uncertainties are now comparable in reflectance to that of MODIS Collection 6 equivalent bands (within 2%) although radiance differences could be larger for several bands, while an agreement on the order of 0.1 K has also been achieved for the thermal emissive bands, except for bands with significant spectral differences or certain bands at extreme temperatures (below 200 K or above 343 K). The degradation in the VIIRS rotating telescope assembly mirrors is gradually leveling off after reaching ~30% and thus far has limited impact on instrument performance and products. Environmental data record users are generally satisfied with the VIIRS data quality which meets the product requirements. While the specific technical details are documented in other papers in this special issue and in Cao et al. (2013a), this paper focuses on the major findings of VIIRS calibration and validation since launch, radiometric performance validation, and uncertainties, as well as lessons learned.

1. Introduction

[2]   The Visible Infrared Imaging Radiometer Suite (VIIRS) is one of the key instruments on the Suomi National Polar-orbiting Partnership (Suomi NPP) satellite designed primarily to observe clouds and earth surface variables. The successful launch of the Suomi NPP Satellite on 28 October 2011 with the VIIRS starts a new generation of capabilities in operational environmental remote sensing for weather, climate, ocean, and other environmental applications. As discussed in more detail in previous publications [*Lee et al.*, 2006; *Hutchinson and Cracknell*, 2006; *Murphy et al.*, 2006; *Cao et al.*, 2013a], VIIRS succeeds the NOAA AVHRR, NASA EOS MODIS,

SeaWiFS, and Defense Meteorological Satellite Program (DMSP) Operational Linescan System (OLS) with 22 spectral bands covering wavelengths from 0.4 to 11.8 μm, providing data for the production of more than 20 Environmental Data Records (EDRs) (Tables 1 and 2) with its calibrated and geolocated Sensor Data Records (SDR).

[3]   The strategic significance of VIIRS cannot be overstated. VIIRS started producing high-quality global data at a time such data are critically needed. First, there is an increasing concern with the aging of the Moderate-Resolution Imaging Spectroradiometer (MODIS) because it has far exceeded their initial design life. Second, the last and final AVHRR for the afternoon orbit was launched on 6 February 2009, after more than 30 years of excellent service. Third, the SeaWiFS and MERIS are no longer available for producing ocean color data. The Landsat family of instruments has limited swath width (185 km). While the thermal infrared images have high spatial resolution (60 m for Landsat 7 at nadir and 100 m for LDCM), the noise performance requirement is relatively low, on the order of 0.4 K at 300 K, compared to the VIIRS thermal imager of better than 0.1 K at 300 K with 375 m spatial resolution. Last but not the least, there is a great need to enhance the nighttime imaging capabilities of the OLS on DMSP satellite, fulfilled by the VIIRS Day Night Band (DNB). In addition to the VIIRS on

[1]STAR, NESDIS, NOAA, College Park, Maryland, USA.
[2]NASA GSFC, Greenbelt, Maryland, USA.
[3]Department of Astronomy, University of Maryland, College Park, Maryland, USA.
[4]CIRA, Colorado State University, Fort Collins, Colorado, USA.
[5]ERT, Inc., College Park, Maryland, USA.

Corresponding author: C. Cao, 5825 University Research Ct., Suite 3250, College Park, MD 20740, USA. (Changyong.Cao@noaa.gov)

Table 1. VIIRS Environmental Data Records

Category	Environmental Data Records
Land	Active Fires
	Land Surface Albedo
	Land Surface Temperature
	Ice Surface Temperature
	Snow Ice Characterization
	Snow Cover
	Vegetation Indices
	Vegetation Health Index
	Green Vegetation Fraction (Priority 2[a])
	Surface Type
	Net Heat Flux
Ocean	Sea Surface Temperature (Priority 2[a])
	Ocean Color/Chlorophyll (Priority 2[a])
Imagery and Clouds	Imagery (Key Performance Parameters = Priority 1[a] for six selected bands: I1, I4, I5, M14, M15, and M16)
	Cloud Optical Thickness
	Cloud Effective Particle Size
	Cloud Top Pressure
	Cloud Top Height
	Cloud Top Temperature
	Cloud Base Height
	Cloud Cover/Layers
	Cloud Mask
	Polar Winds (Priority 2[a])
Aerosols	Aerosol Optical Thickness
	Aerosol Particle Size
	Suspended Matter

[a]Priority 1 products include VIIRS SDR and Imagery for six selected bands (Source: JPSS (2013), L1RD V2.7, 30 January 2013).

Suomi NPP, which is already in orbit, the VIIRS for the J1 and J2 follow-on missions are currently being developed for the next decade. Therefore, the success of the VIIRS on Suomi NPP has many profound impacts on earth observations.

[4] VIIRS was turned on 8 November 2011 for the uncooled Reflective Solar Bands (RSB), with the nadir door opened on 21 November 2011, while the VIIRS cryo-cooler door was opened on 18 January 2012, starting the observations in the cooled RSB and Thermal Emissive Bands (TEB). Preliminary assessment of the VIIRS onboard performance indicates that VIIRS not only significantly outperforms the legacy operational sensor AVHRR in spatial, spectral, and radiometric quality but also outperforms MODIS in several aspects. This paper summarizes the VIIRS verification and validation efforts since launch. Sections 2 and 3 discuss the VIIRS sensor characteristics and performance. Section 4 presents an overview of the VIIRS postlaunch calibration/validation activities. The validation of the VIIRS SDR is summarized in section 5. Section 6 introduces the long-term monitoring. Lessons learned as well as remaining issues are presented in section 7, followed by conclusions. Other aspects of postlaunch activities such as geolocation validation, calibration methodologies, and maneuvers are discussed in separate papers in this special issue on Suomi NPP.

2. The VIIRS Instrument and SDR Characteristics

[5] VIIRS provides global moderate-resolution data twice daily without any gap. It is a scanning radiometer with a total field of regard of 112.56° in the cross-track direction. At a nominal equatorial altitude of 829 km, the swath width is ~3060 km, providing full global daily coverage both in the day and night side of the Earth. The VIIRS scan pattern, block diagram, and channel characteristics have been well documented in previous publications [*Hutchinson and Cracknell*, 2006; *Wolfe et al.*, 2012; *Cao et al.*, 2013a], and therefore only a short summary is provided here. VIIRS has 16 moderate-resolution bands (M bands, each with 16 detectors) with a spatial resolution of 750 m at nadir, five imaging resolution bands (I bands, each with 32 detectors) with a 375 m spatial resolution at nadir, and one panchromatic DNB with a near constant 750 m spatial resolution throughout the scan. The M bands include 11 RSB and 5 TEB. The I bands include 3 RSB and 2 TEB. Generally, the M bands have a better signal-to-noise ratio than the I bands.

[6] VIIRS uses six dual-gain RSB bands with a wide dynamic range needed for ocean color applications, at the same time without saturating the sensor when observing high-reflectance surfaces such as land and clouds. The dynamic range of the dual-gain bands in high gain is comparable to that of the MODIS ocean color bands, while the dynamic range in the low-gain state is comparable to similar MODIS land bands. The dynamic ranges for all other bands are similar to their MODIS counterparts. VIIRS also has a dual-gain TEB band (M13) for both fire detection and sea surface temperature (SST). VIIRS uses a unique approach of pixel aggregation which controls the pixel growth toward the end of the scan—a problem that exists for MODIS, AVHRR, and other instruments. As a result, the VIIRS spatial resolutions for nadir and edge-of-scan data are more comparable. To save transmission bandwidth, VIIRS also uses a "bow-tie" deletion to remove duplicated pixels in the off-nadir regions where pixels overlap between adjacent scans. This however introduces some visual artifacts in the raw image beyond midscan [*Wolfe et al.*, 2012; *Cao et al.*, 2013a].

[7] In addition to the novel geometric characteristics of VIIRS, the VIIRS DNB is effectively a calibrated radiometer. Figure 1 shows a sample image of the VIIRS DNB over the hurricane Sandy on 30 October 2012. This occurred near full moon (lunar phase angle of 5.15°, lunar zenith angle 34°) so that the cloud reflection of the moonlight from the hurricane is clearly observed. Unlike the imaging bands, the DNB has a near constant spatial resolution of 750 m across the entire scan, which is achieved by using 32 aggregation modes. Similar to the RSB calibration, the DNB band is calibrated using the solar diffuser, along with dark samples of earth view during new moon. This allows much more accurate calibrated radiances than the predecessor OLS which has no onboard calibration. In addition, the OLS sensor saturates in urban areas with intense lights. It is estimated that the city light in the Manhattan, New York has a typical mean clear sky night radiance of about 200 nano watts per square centimeter per steradian (nW/(cm^2 sr)), while on this image the radiance is only about 32 nW/(cm^2 sr) due to clouds, including reflected moonlights. Using a lunar model [*Miller and Turner*, 2009], the radiance is further separated into reflected lunar radiance 22.5 nW/(cm^2 sr) and transmitted/scattered city lights 9.5 nW/(cm^2 sr). By comparison, the downtown Chicago area (on the edge of the Hurricane in this image) has relatively clear sky in this image, and the radiance is on the order of 99 nW/(cm^2 sr). Given the absolute radiometric calibration uncertainty of 3–11% depending on the radiance level (high uncertainty at low radiances) (L. Liao et al., Suomi NPP VIIRS Day and Night Band (DNB) Performance, submitted

Table 2. VIIRS Spectral Band Characteristics

Band No.	Center Wavelength (μm)	Equiv. Width (μm)	Esun[a] (W/m² μm)	Esun[b] (W/m² μm)	Driving EDR(s)	Band Gain	Ltyp or Ttyp (Spec)	Lmin or Tmin	Lmax or Tmax	Spec SNR or NEdT (K)	On Orbit SNR or NEdT (K)	MODIS Equiv. Band
VisNIR												
M1	0.411	0.0198	1709.63	1708.68	Ocean Color Aerosol	H	44.9	30	135	352	588	B8
						L	155		615	316	1045	
M2	0.444	0.0143	1902.51	1862.88	Ocean Color Aerosol	H	40	26	127	380	572	B9
						L	146		687	409	1010	
M3	0.486	0.0190	1988.69	1999.76	Ocean Color Aerosol	H	32	22	107	416	628	B10
						L	123		702	414	988	
M4	0.551	0.0209	1842.40	1869.63	Ocean Color Aerosol	H	21	12	78	362	534	B4/B12
						L	90		667	315	856	
I1	0.639	0.0775	1604.83	1628.43	Imagery EDR	S	22	22	718	119	214	B1
M5	0.672	0.02	1504.55	1530.12	Ocean Color Aerosol	H	10	9	59	242	336	B13/B1
						L	68		651	360	631	
M6	0.745	0.0146	1277.38	1280.77	Atmosph. Correct.	S	9.6	5.3	41	199	368	B15
I2	0.862	0.0394	961.64	962.82	NDVI	S	25	25	349	150	264	B2
M7	0.862	0.0387	961.28	962.46	Ocean Color Aerosol	H	6.4	3.4	29	215	457	B16/B2
						L	33.4		349	340	631	
S/MWIR												
M8	1.238	0.0271	455.97	456.87	Cloud Particle Size	S	5.4	3.5	165	74	221	B5
M9	1.375	0.0150	366.15	360.22	Cirrus/Cloud Cover	S	6	0.6	77.1	83	227	B26
I3	1.602	0.0572	251.35	245.79	Binary Snow Map	S	7.3	7.3	72.5	6	149	B6
M10	1.602	0.0587	250.86	245.30	Snow Fraction	S	7.3	1.2	71.2	342	586	B6
M11	2.257	0.0467	77.31	75.07	Clouds	S	0.12	0.12	31.8	10	22	B7
I4	3.753	0.360			Imagery Clouds	S	270	270	353	2.5	0.4	B20
M12	3.697	0.192			SST	S	270	230	353	0.396	0.12	B20
M13	4.067	0.165			SST/Fires	H	300	210	343	0.107	0.04	B23
						L	380		634	0.423		
LWIR												
M14	8.578	0.324			Cloud Top Properties	S	270	190	336	0.091	0.06	B29
M15	10.729	0.990			SST	S	300	190	343	0.07	0.03	B31
I5	11.469	1.75			Cloud Imagery	S	210	270	340	1.5	0.4	B31
M16	11.845	0.866			SST	S	300	190	340	0.072	0.03	B32

[a]In-band solar irradiance computed using Thuillier 2003 spectra.
[b]In-band solar irradiance computed using the operational IDPS version as of 2013 (originated from MODTRAN4.3).
Center wavelength and equivalent band width are computed based on the IDPS version of the VIIRS RSR (https://cs.star.nesdis.noaa.gov/NCC/SpectralResponseVIIRS).
Equivalent width is defined as the band width of a rectangular function whose height is equal to the maximum of the RSR, and its area is equal to the area under the RSR curve. Given that the RSR is normalized to 1.0, the equivalent width therefore equals the integral of the RSR. Center wavelength is defined as the wavelength which equally divides the area under the RSR into one half.
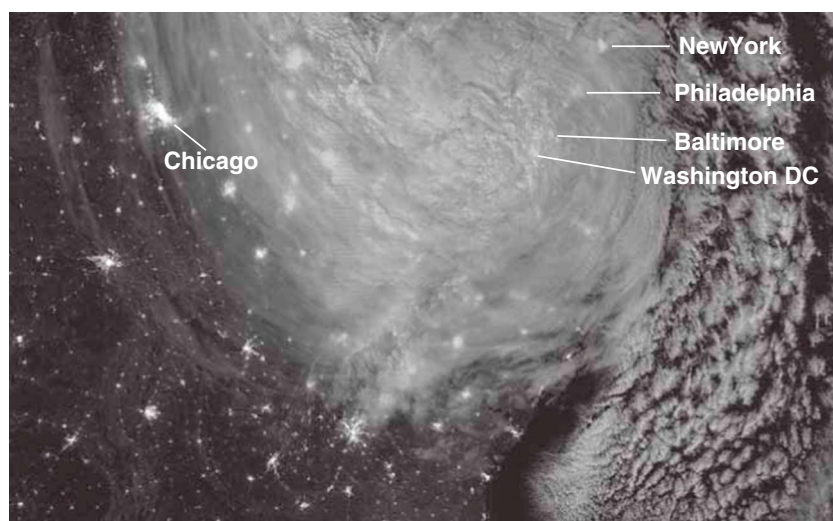
Figure 1. Example VIIRS DNB image over the hurricane Sandy on the east coast on 30 October 2012.

to *Journal of Geophysical Research: Atmospheres*, 2013), it is expected that these radiance values are comparable not only spatially between cities and sites but also temporally in time series analysis. The ability to accurately calibrate the radiances in the DNB is a major step forward, which will enable and/or enhance a number of quantitative applications [*Lee et al.*, 2006]. The success of the VIIRS with the DNB has inspired a number of new applications including air glow, aerosols, aurora, lightning, as well as enhanced existing applications such as correlating city lights with power consumption and greenhouse gas, smoke and fire, fishing boats, urban expansion [*Miller et al.*, 2012; *Doll et al.*, 2006; *Chand et al.*, 2009; *Zhuo et al.*, 2009], and detection of light loss due to severe weather [*Cao et al.*, 2013b].

[8] With a 375 m spatial resolution, the VIIRS thermal imaging bands have significantly outperformed both MODIS and AVHRR and allow a moderate-resolution sensor to observe

manmade features such as harbors, canals, and bridges. Figure 2 is an example VIIRS I5 image (12 µm), which shows the coastal aquaculture on the east coast of China, an area known for seaweed farming [*Shang et al.*, 2008], land reclamation and coastal landfills. The VIIRS thermal imaging bands may potentially be used to monitor aquaculture production.

[9] More detailed characteristics of VIIRS image can be observed from Figure 2, which is made from two granules (each granule has 1536 scan-lines for the imaging bands). The imaging bands have 6400 pixels across scan within a scan angle of ±56.28° from nadir. The spatial resolution of 375 m at nadir grows to 800 m at the end of the scan. This pixel growth rate is considerably smaller than those of the heritage sensors, which grow at a ratio greater than four times [*Lee et al.*, 2006; *Cao et al.*, 2013a]. The interleaving blank lines starting from scan angle 31.72 to 56.28° are due to the bow-tie deletion to save transmission band width by design.
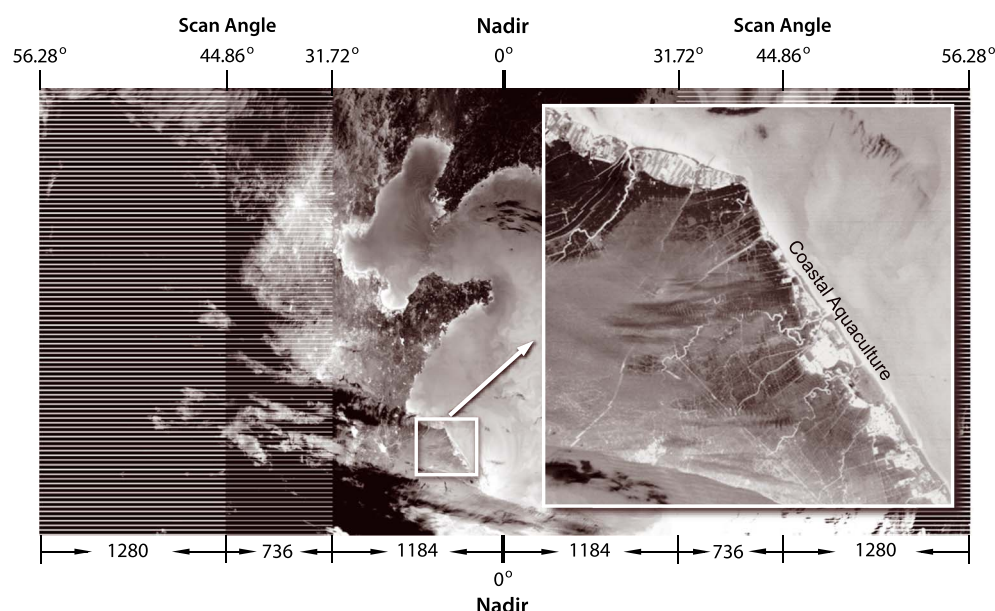

Figure 2. Example VIIRS I5 image with 375 m resolution on 16 April 2012.
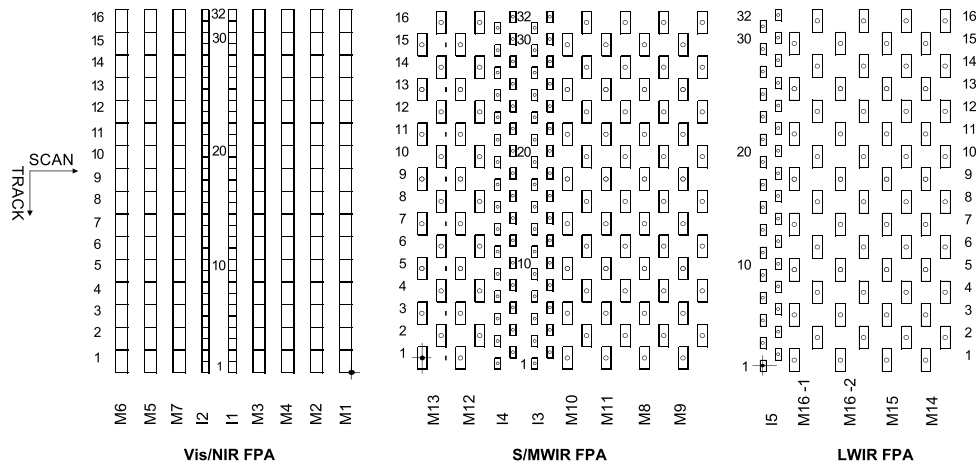
Figure 3. VIIRS focal plane array layout (source: VIIRS calibration ATBD).

From nadir to scan angle 31.72° (zone 1), the 1184 in-scan samples are aggregated at a ratio of 3:1, but no bow-tie deletion is performed in the track direction. From scan angle 31.72 to 44.86° (zone 2), the 736 samples are made by aggregating 2 pixels each in the scan direction, while four rows (two leading and two trailing) are deleted for the bow-tie effect. From scan angle 44.86 to 56.28° (zone 3), no aggregation is performed on the pixels in the scan direction, while eight rows are deleted in the track direction for the bow-tie removal. It should be noted that the bow-tie deletion and aggregation are performed on the spacecraft for the single-gain bands, while this is done on the ground for the dual-gain bands. Also note that for the M bands, the dimensions in the scan and track directions are exactly half of those for the imaging bands.

[10] At the VIIRS focal plane, each M band has 16 detectors, while each I band has 32 detectors in the along-track direction (Figure 3, showing in sensor order). These detectors in the visible/near-infrared (VIS/NIR) are rectangular with the smaller dimension in the along-scan direction. While in the Short-Mid-Long-wave infrared (SWIR/MWIR/LWIR), they are octagonal in shape but made rectangular with the microlens. The design takes into account the different growth rates in the scan and track directions. As the rotating telescope assembly (RTA) scans the Earth, these detectors sweep out a swath from scan angle −56.28° to +56.28°. Note that the I band pixels are nested into the M band pixels with a 2:1 ratio in both along-scan and along-track directions.

3. VIIRS Radiometric Performance Requirements and Onboard Calibration

[11] High level requirements of the VIIRS performance can be found in the Joint Polar Satellite System (JPSS) Level 1 requirement document (L1RD). Major radiometric requirements of VIIRS are shown in Table 2. The radiometric accuracy requirement is 2% in reflectance of Ltyp (typical scene radiance) for the RSB from 0.4 to 2.25 μm. There is also a polarization sensitivity requirement of 3% for the 0.4 μm and 0.86 μm bands, and 2.5% for the rest of the M bands below 1 μm. The Field of View (FOV) at nadir is required to be better than 0.8 km for the M bands and 0.4 km for the I bands, while this requirement is relaxed to 1.6 and

0.8 km at end of the scan for the M and I bands, respectively. The dynamic range and other requirements are also shown in Table 2.

[12] To meet the radiometric requirements, the VIIRS design incorporates onboard calibration devices inherited from MODIS: the solar diffuser (SD) and solar diffuser stability monitor (SDSM) for the RSB, and the blackbody for the TEB [*Guenther et al.*, 2002; *Cao et al.*, 2013a; *Xiong et al.*, 2013]. Fundamentally, this is a traditional calibration approach using two calibration points: the On-Board Calibration Blackbody (OBCBB), and SD as the high points for the TEB and RSB bands respectively, and space view (SV) for offset subtraction for both. The SD is illuminated once per orbit as the satellite passes from the dark side to the sunlit side of the Earth near the South Pole. An attenuation screen covers the opening, but there is no other optical element between the SD and the sun. The bidirectional reflectance distribution function (BRDF) of the SD and the transmittance of the attenuation screen are measured prelaunch and updated on orbit using data collected during spacecraft yaw maneuvers. Given the angle of incidence, the reflected radiance of the sun can be computed and is used as a reference to produce calibrated reflectance and radiance.
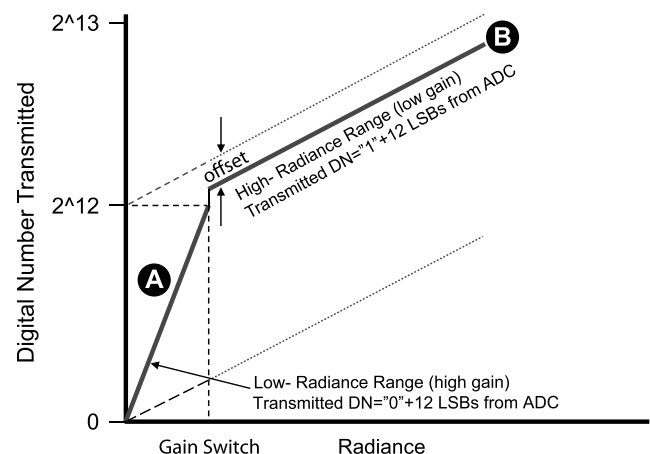

Figure 4. VIIRS dual-gain band and gain switching.

Table 3. VIIRS Postlaunch Cal/Val 57 Tasks

Task Category	Task ID	Title	Task Category	Task ID	Title
Functional Performance and Format (FPF) Evaluation	FPF-1	Noise measurement prior to RTA scanning	Performance and Telemetry Trending (PTT)	PTT-1	Operability, noise, SNR verification
				PTT-2	RDR histogram analysis
	FPF-2	Operability, noise, SNR verification with nadir door closed		PTT-3	Noise and SNR for uniform EV scenes
	FPF-3	In-scan aggregation verification—non-DNB bands		PTT-4	DNB offset verification
	FPF-4	Dual-gain band and DNB transition verification		PTT-5	Electronic gain measurement
	FPF-5	Onboard bow-tie deletion verification	Radiometric Evaluation (RAD)	RAD-1	Out-of-band (OOB) spectral leakage
	FPF-6	DC-restore functionality and performance check		RAD-2	Crosstalk from emissive bands to reflective bands
	FPF-7	Calibrator visual inspection		RAD-3	Dynamic range and linearity
Calibration System Evaluation (CSE)	CSE-1	SD and SDSM characterization		RAD-4	Response vs. Scan angle (RSB)
	CSE-2	Onboard calibrator black body (OBCBB) temperature uniformity		RAD-5	Relative band-to-band calibration analysis using lunar data[a]
	CSE-3	Straylight VIIRS RSB solar diffuser stray light—analysis of nonpolar SD data[a]		RAD-6	Relative band-to-band calibration analysis using SD data[a]
	CSE-4	Temporal analysis of SD signal over polar region		RAD-7	SDR comparison with model
	CSE-5	Temporal analysis of SDSM data		RAD-8	SDR comparison with AVHRR
	CSE-6	Yaw maneuver analysis—solar attenuation screen (SAS) transmission		RAD-9	SDR comparison with MODIS
	CSE-7	Analysis of SDSM data with model assisted extrapolation of screen calibration data[a]		RAD-10	RSB radiance/reflectance validation—radiometric sites
Image Quality Evaluation (IMG)	IMG-1	Crosstalk, echo, and ghost investigation		RAD-11	TEB validation using lake Tahoe site
	IMG-2	Image analysis (striping, glints and other artifacts)		RAD-12	In-band spectral radiance comparison with CrIS
	IMG-3	Moon echo and ghost check		RAD-13	TEB SDR band-to-band radiometric comparison
	IMG-4	LSF/MTF validation[a]		RAD-14	Structured scene analysis
Geometric Evaluation (GEO)	GEO-1	Initial validation of SC auxiliary ephemeris and attitude data		RAD-15	Emissive band response characterization
	GEO-2	Initial validation of VIIRS encoder data, scan time, scan period, and scan rate stability		RAD-16	Moon in space view correction
	GEO-3	Assess reasonableness of first-period SDR geolocation		RAD-17	Band-to-band registration (BBR) verification
	GEO-4	Build first-period simulated VIIRS images from GCP chips		RAD-18	RSB radiance/reflectance validation—underflights
	GEO-5	Build first-period VIIRS image chips from selected SDR pixels		RAD-19	Lunar data analysis—roll maneuver
	GEO-6	Perform first-period VIIRS simulated image match-up		RAD-20	Spectral validation using hyperspectralData from aircraft underflights
	GEO-7	Analyze first-period VIIRS GCP residuals		RAD-21	TEB validation with NAST-I and MAS underflights
	GEO-8	Analyze initial intraorbit thermal effects on geolocation		RAD-22	Analysis of pitch maneuver data (TEB RVS)
	GEO-9	Develop and test initial geolocation parameter & thermal LUT updates		RAD-23	SDR reprocessing and updates
				RAD-24	RSB and TEB SDR accuracy—provisional and validated levels
				RAD-25	Dual-gain anomaly flagging verification[a]

[a]Not essential for provisional maturity.

Since the SD may degrade over time, the SDSM is used to compare the directly measured sunlight to that reflected from the SD, providing a means of monitoring the degradation of the SD throughout the entire mission. Lunar calibration through spacecraft roll maneuver is part of the postlaunch calibration strategy to ensure that the sensor degradation is independently validated. The SDR radiometric calibration algorithms convert raw data records (RDRs) in digital numbers (DNs) from Earth view observations into SDR radiance, reflectance, and brightness temperature products.

[13] The TEB are calibrated using the OBCBB which was carefully characterized prelaunch. The OBCBB emissivity is estimated to be 0.996 for the TEB bands. The OBCBB temperature is carefully controlled using heater elements and thermistors. The calibration algorithm, based on measured OBCBB temperature and emissivity, computes the gain

based on radiances and instrument output counts. Because of emissive background variations caused by components in the surround, additional corrections must be made, such as for the scan angle dependent responses. Knowledge of spacecraft ephemeris, alignment, and instrument scan rate are used to geolocate the sensor data with high accuracy. The combined calibrated radiances with geolocation comprise the SDRs.

[14] The VIIRS radiometric calibration algorithm is implemented as part of the VIIRS data processing software in order to convert raw digital numbers (DN) from EV observations into the various SDR radiance products. As part of this algorithm, DNs from the OBCBB, SV, and SD view are processed in order to adjust DNs for background signal levels and to update reflective band and emissive band calibration coefficients. Detailed methodologies can be found in the VIIRS Algorithm Theoretical Basis Document and in *Xiong et al.* [2013].

[15] Understanding the dual-gain mechanism is very important for VIIRS calibration (Figure 4). The dual-gain bands are calibrated for both gain states using the SD by scanning the SD in high and low gains in sequence. Transitions from high gain (low radiance) to low gain (high radiance) are performed automatically at the focal plane electronics level based on a switch point bias voltage that is supplied by the Analog Signal Processor, which is a component of the Electronics Module.

[16] Figure 4 shows schematically DN versus radiance and the switchover from high gain to low gain. Note that for any particular DN, there is only one radiance value (along the A-B line). The most significant bit of the 13 bits is used for dual gain to flag the low-gain mode. Because the gain and offset are different between the gain modes, calibration is performed individually for each mode, and thus a separate space view and calibration source view (OBCBB or SD). Since calibration is also performed separately for each mirror side, the dual-gain bands require four scans to complete a calibration cycle.

4. Overview of Postlaunch Calibration/Validation

[17] The VIIRS RSB calibration started as soon as the VIIRS sensor was turned on. The TEB calibration followed after the VIIRS cryo-cooler door was opened. Intensive calibration and validation are carried out when the JPSS operational ground system Interface Data Processing Segment (IDPS) started processing and producing the VIIRS SDR data. The VIIRS calibration and validation are comprehensive and were divided into 57 tasks (Table 3), carried out by different organizations (F. Deluccia and C. Cao, "VIIRS SDR calibration/ validation operations concept (OPSCON) document", JPSS program document, unpublished data, 2011). With the completion of these tasks, the VIIRS SDR has progressively achieved high levels of maturity (from beta to provisional, and eventually to calibrated/validated).

[18] The Functional Performance and Format (FPF) evaluation was conducted shortly after launch, and all seven FPF tests were verified successfully with no issues. This verification is significant given the complex operations of bow-tie deletion, aggregation, and dual-gain handling. The comparison of noise before and after RTA scanning required a longer

evaluation and is discussed in more detail in the long-term monitoring section.

[19] The Calibration System Evaluation (CSE) required a much longer time period than expected due to several complications. As discussed in detail in previous publications [*Fuqua et al.*, 2012; *Iona et al.*, 2012; *Deluccia et al.*, 2012; *Cao et al.*, 2013a], there is a major anomaly with the VIIRS RTA degradation in particular near the 0.86 μm bands such as M7. Investigation of the VIIRS anomaly identified the root cause as tungsten oxide contamination, deposited on the surface of the mirror. Tungsten oxide leads to the darkening of the surface of the mirror when exposed to ultraviolet radiation from the sunlight [*Johnston*, 2000]. Investigation revealed that a nonstandard process occurred during the mirror coating as a potential source of tungsten oxide contamination. With witness samples, the mirror darkening rate was simulated. However, despite this anomaly, model predictions suggest that the VIIRS will still meet its performance requirements within the 7 year design life due to its large performance margins [*Murgai et al.*, 2012].

[20] In addition to the RTA mirror degradation, there is also significant degradation in the Solar Diffuser due to long exposure to the sun light, and degradation in the Stability Monitor (SDSM) detectors. Decoupling these degradations required long time period of data with time series analysis. Maneuvers are also required to better characterize the solar attenuation screen transmission function. A small nonuniformity on the order of 0.05 K was also found in the onboard calibrator blackbody as discussed in the long-term monitoring section. Nevertheless, all tasks were completed by 5 April 2012 when the VIIRS SDR reached beta maturity status.

[21] In Image Quality Evaluation (IMG), the VIIRS images were found to be of high quality, with minimal artifacts. This is in contrast to the early days of MODIS where crosstalk and striping were significant issues. Despite concerns about uneven polarization response among the detectors revealed in prelaunch, striping was found to be insignificant postlaunch. Exceptions exist in the DNB due to stray light contamination (Liao et al., submitted manuscript, 2013), and minor striping in other bands over highly uniform scenes such as over ocean and snow surfaces, which will require further investigation in the near future. Also, certain striping during day time at high scan angles was found to be due to view geometry variations, as discussed in the validation section. Limited validation of the Line Spread Function (LSF) and Modulation Transfer Function (MTF) has been performed, due to the lack of suitable targets for low resolution sensors. As a result, evaluations of LSF and MTF are preliminary, and the investigation is ongoing [*Wolfe et al.*, 2012].

[22] The Geometric Evaluation team has quickly resolved several issues and reduced the geolocation error from the initial ~1 km shortly after launch down to ~80 m, or a quarter of an imaging band pixel by April 2012. The team has overcome several complications in the process due to scan electronics side changes, scan mirror sync loss, maneuvers, ephemeris availability, and uncertainties.

[23] The signal-to-noise ratio (SNR) computed from on-orbit solar diffuser data for the RSB are comparable to those from prelaunch data and well within the specifications. However, due to the unexpected RTA mirror degradation, the SNR for channels affected by the RTA mirror degradation are decreasing over time. For example, the M7 low-
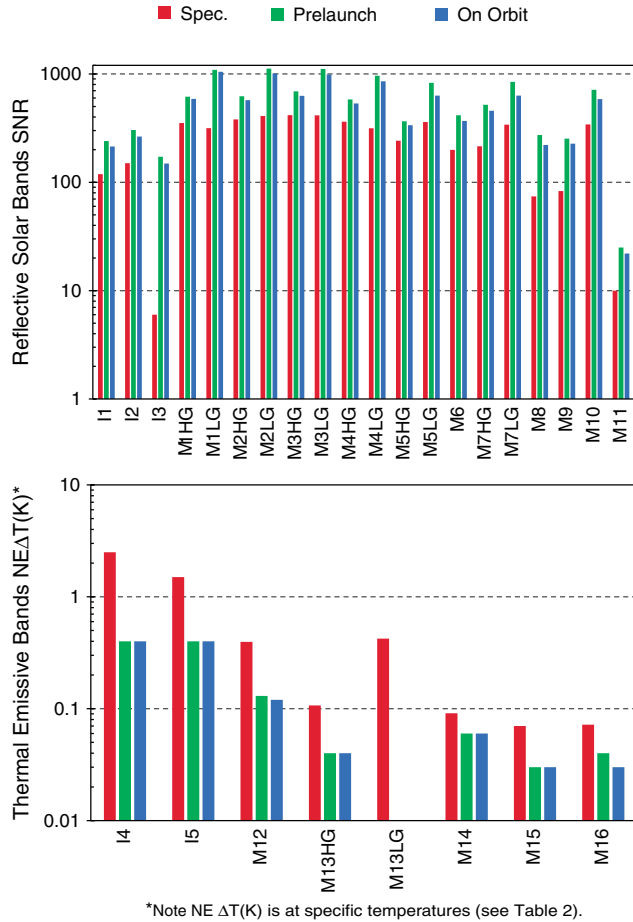
Figure 5. VIIRS band noise performance.

gain SNR decreased from 631 in April 2012, to 551 by September 2012 [*Cao et al.*, 2013a]. Based on the mirror degradation model, it is expected that the SNR will still meet the instrument specification by the end of the VIIRS 7 year mission. Since the degradation is spectrally dependent, it is modulating the effective spectral response function for the bands affected. However, current estimate shows that as long as the calibration lookup tables are updated accordingly in response to the degradation, the radiometric and spectral impacts of the degradation on products would be negligible (with the exception of DNB, which has a very broad spectral response).

[24] A major effort in the postlaunch Cal/Val is the radiometric evaluation, which has the largest number of tasks among the six categories shown in Table 3. Given the significance of this topic, the next section discusses the radiometric validation of VIIRS SDR in more detail. Also, several discrepancies were found in the Cal/Val process which may still have implications for the VIIRS SDR radiometric accuracy, such as the source for the solar spectral irradiance, as discussed in section 7.

[25] Finally, reprocessing is considered out of the current scope of the calibration/validation and therefore will have to be investigated later. While this has minimal impacts on products relying on timely satellite data, it may have significant impacts on time series analysis. For example, the ocean color team has tested the reprocessing using different versions of the calibration lookup tables and found discrepancies in the

trends compared to the Marine Optical Buoy (Wang and Shi, personal communications, 2013). Therefore, reprocessing all VIIRS data since launch with the best calibration available to ensure its consistency and accuracy is still a desirable goal.

5. Radiometric Validation of the VIIRS SDR

[26] Radiometric noise, accuracy, uncertainty, and their long-term changes are important issues in validating VIIRS. All VIIRS bands have excellent noise performance based on postlaunch Cal/Val using onboard calibrators, as shown in Figure 5 and discussed in detail in *Cao et al.* [2013a] and *Xiong et al.* [2013]. However, the 2% in reflectance absolute radiometric accuracy for the RSB of VIIRS needs to be validated by independent means. Similarly, the TEB require independent validation to ensure that the instrument meet specifications. To address these issues, the VIIRS SDRs are compared with that of MODIS and CrIS at the Simultaneous Nadir Overpass (SNO) and vicarious sites. Although intercomparison with aircraft under-flight was in the original plan, this task was delayed due to funding constraints, and only limited studies will be performed in 2013.

[27] SNOs between two satellite instruments occur when their nadirs meet at the orbital intersection within a small time window, which occurs periodically for two satellites flying at different altitudes and provides excellent opportunities for radiometer intercomparisons [*Cao and Heidinger*, 2002, *Heidinger et al.*, 2002, *Cao et al.*, 2004]. SNOs usually occur at high-latitude polar regions. However, for Suomi NPP VIIRS and Aqua MODIS, SNOs occur at both high and low latitudes due to similar equator crossing times. Intercomparison between VIIRS and MODIS was performed using the SNO approach at both polar and low latitude regions over ocean and desert.

[28] Early SNO intercomparisons in 2012 revealed that large biases on the order of 5% existed between VIIRS M1 and Aqua MODIS B8. After a thorough investigation, it was concluded that the bias was due to a MODIS calibration drift for this blue band in MODIS collection 5. This bias disappeared when the new MODIS collection 6 data were used in the comparison (Figure 6a). As a result, MODIS collection 6 has been used for all subsequent comparisons. Note that this validation focuses on M1–M8 and I1–I2 bands. M10 and M11 cannot be validated effectively because the matching MODIS band (band 6) for M10 has many inoperable detectors, M11 covers very different spectral region compared to the MODIS equivalent band, while M9 is difficult to validate because its spectral response function is significantly different from that of MODIS B26, and this band is sensitive to water vapor which varies greatly in both time and space. Further validations for these three bands are needed in the near future.

5.1. Comparisons at SNOs in the Low Latitude

[29] VIIRS and MODIS intercomparisons are performed in the low latitudes over the North African desert. Near nadir overlapping region between MODIS and VIIRS observations are compared for M bands M1 through M8 excluding M6 (saturated on desert scenes). For each SNO-*x* event, VIIRS reflectance data are mapped to MODIS pixel-by-pixel. Then collocated multiple regions of interest (ROI) are cloud
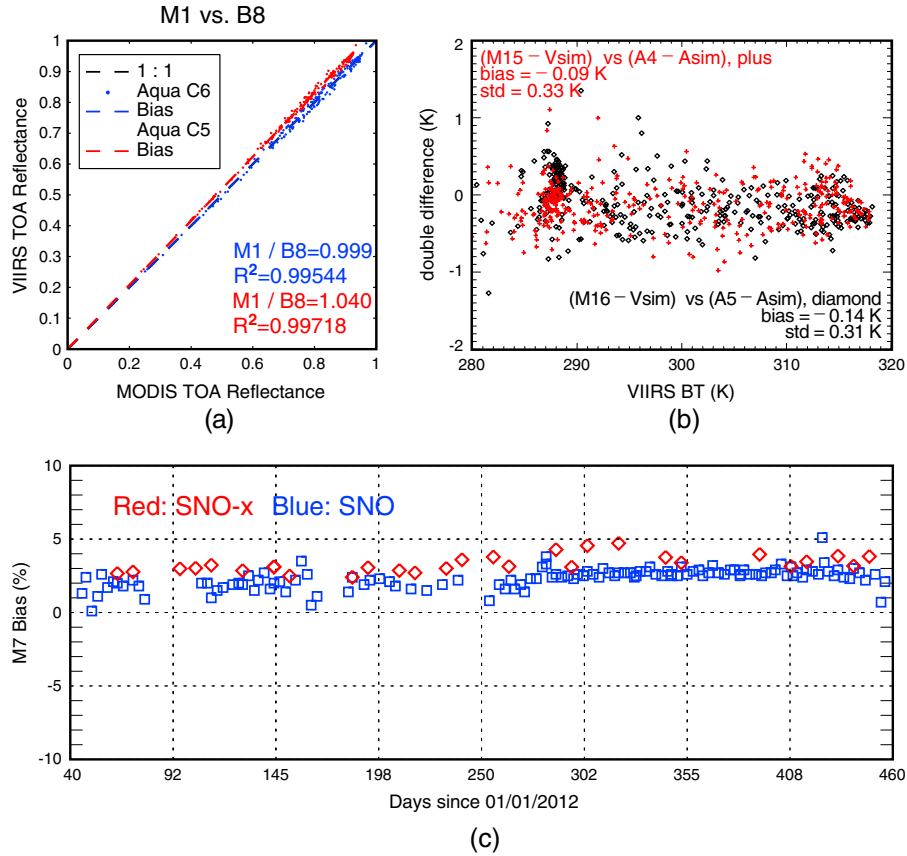
Figure 6. VIIRS and MODIS radiometric comparisons: (a) M1 comparison with MODIS B8 collection 5 versus 6; (b) comparisons for the SST bands; (c) radiometric bias time series between VIIRS and MODIS: Bias = (VIIRS-MODIS)/MODIS.

screened using VIIRS and MODIS cloud mask data and spatial uniformity test. The data within the ROIs (with a size of 9 km × 9 km each) are extracted at near nadir for each sensor. The average reflectance of each ROI is calculated for both VIIRS and MODIS, and the bias between them is then derived. For each SNO-*x* event, the mean and standard deviation of the biases are computed and plotted as a time series to evaluate the relative radiometric performance of VIIRS.

[30] Figure 6c shows the radiometric bias time series of VIIRS band M7 relative to the MODIS matching band 2 from early March 2012 till the end of March 2013. The uncertainty in the bias trend is estimated to be 1% for the time series. It is noted that in early April 2012, the SD attenuation screen data were updated once. This update in the lookup table (LUT) caused sudden drops in bias for a few VIIRS radiometric bands during this time period. Figure 6c suggests that a ~3% bias exists between VIIRS M7 and MODIS band 2. Investigation reveals that the difference in VIIRS and MODIS RSR and the monotonically increasing desert reflectance spectra are the major causes for the large bias in VIIRS band M7. After accounting for the spectral differences using hyperspectral data and radiative transfer calculations, the biases are much reduced (similar issues also exist for M5). Table 4 shows that the biases for the VIIRS moderate radiometric bands relative to MODIS are mostly within 2% in reflectance by the end of March 2013 with the exceptions of M8 (S. Uprety et al., Radiometric inter-comparison between Suomi NPP VIIRS and Aqua MODIS reflective solar bands

using simultaneous nadir overpass in the low latitudes, submitted to *Journal of Atmospheric and Oceanic Technology*, 2013). Note that additional biases may exist in radiance comparisons for some channels due to the use of different versions of solar irradiance, as discussed in section 7.

5.2. Comparisons at SNOs in the Polar Regions

[31] SNO events between Suomi NPP and Aqua satellites occur at polar regions more frequently with a time difference within a few minutes. Compared to the more than 10 min time difference for SNOs in the low latitudes, the small time difference creates nearly identical viewing conditions (sensor and solar geometry) and greatly reduces the uncertainties in radiometric bias analysis due to the surface BRDF and cloud movements. The intercomparisons are performed for multiple SNOs on the same day with time difference ranging from a few seconds to a few minutes and using the VIIRS and MODIS pixels within a radius of 12.5 km from the SNO position. All SNO data sets acquired by VIIRS and MODIS during daytime since mid-February 2012 were included in the comparisons (Table 4). Polar region does not receive sunlight all year round; therefore, the SNO analysis is performed over the South Pole region during austral summer and North Pole region during summer.

[32] VIIRS radiometric performance for imaging (I1 and I2) and moderate-resolution (M1 through M8) bands have been continuously evaluated since early launch using the SNOs [*Blonski et al.*, 2012]. VIIRS band M6 often becomes

Table 4. VIIRS Mean Reflectance Bias Relative to MODIS at SNOs and Dome C

VIIRS Band	MODIS Band	Bias at Polar SNO	Expected Spectral Bias	Bias at SNO-x	Expected Spectral Bias	Bias at Dome C	Expected Spectral Bias
M1	8	0.00%	0.00%	0.80%	−0.26%	−0.60%	−0.70%
M2	9	0.00%	-	−1.73%	−0.94%	-	-
M3	10	0.00%	-	−1.27%	−0.47%	-	-
M4	4	2.00%	0.50%	−1.49%	−1.63%	0.00%	1.40%
M5	1	5.00%	2.50%	10.25%	7.80%	4.30%	3.50%
M6	15	0.50%	-	-	-	-	-
M7	2	2.50%	0.50%	4.01%	1.56%	3.30%	1.70%
M8	5	5.00%	0.50%	3.45%	0.18%	4.30%	5.30%
I1	1	0.00%	−0.50%	-	-	-	-
I2	2	2.50%	0.50%	-	-	-	-

The polar SNO data were acquired between February 2012 and May 2013 (every 2–3 days). In total, 167 SNO events with Aqua MODIS were included in the analysis, but due to saturation, 164 points were used for the M7/B2 and 166 points used for the M1/B8 comparisons.

SNO-x is for SNO in the low latitudes over the N. African desert. Data were taken from the end of February 2012 to the end of March 2013. A total of 28 clear sky SNO-x events at North African Deserts were used out of 44 events collected (every 8 days apart).

Spectral Bias for polar SNO is computed for snow using the 6S radiative transfer model.

Spectral Bias for SNO-x is computed using both MODTRAN (M1) and Hyperion observations (M2 to M8).

Estimated bias uncertainty: SNO: ±0.5%; SNO-x: ±1%.

The large bias for M5 is primarily due to RSR differences between MODIS and VIIRS.

M8 indicates a large bias relative to Aqua/MODIS. However, M8 bias is near zero relative to Terra MODIS.

saturated over snow and thus only a few SNO events have been analyzed. The major difference between the SNO at polar region and the SNO in the low latitudes is that, in the polar area, VIIRS and MODIS are compared at the exact orbital intersection rather than at the orbital overlapping areas. Figure 6c shows that the VIIRS bias relative to MODIS observed at the SNO in the polar region is consistent with those at the low latitudes. VIIRS radiometric bias in reflectance relative to MODIS is less than 2% for all imaging and radiometric bands except band M8 which has a bias of nearly 3% due to large spectral differences between MODIS and VIIRS.

5.3. Validation at Vicarious Calibration Sites

[33] In addition to SNOs, VIIRS on-orbit radiometric stability and bias are routinely monitored using stable vicarious calibration sites such as deserts, and the Dome C in the Antarctica. Dome C is a spectrally and radiometrically stable large snow flat located near the South Pole at −75.1° latitude and 123.35° longitude. This site has been frequently used for the calibration/validation of visible near-infrared radiometers [*Loeb*, 1997; *Six et al.*, 2004, *Cao et al.*, 2010, *Uprety and Cao*, 2012]. VIIRS and MODIS nadir measurements over Dome C are collected regularly during austral summer. An ROI size of 40 km × 40 km is chosen with Dome C latitude/longitude as the center. Spatial uniformity test is performed for cloud screening. Mean TOA reflectance of VIIRS and MODIS bands are calculated and compared to estimate the radiometric bias of VIIRS relative to MODIS. At Dome C, VIIRS observations agree with MODIS within 2% in reflectance for most of the bands except VIIRS band M8. The bias estimated at Dome C agrees well with the bias estimated at the polar and low latitude SNOs.

5.4. VIIRS TEB Validation

[34] VIIRS TEB are validated against the AVHRR, MODIS, and CrIS data with SNO observations. CrIS is a hyperspectral sensor and its data can be convoluted with the VIIRS spectral response function to simulate the VIIRS band radiance. While VIIRS M13, M15, and M16 are nearly fully covered spectrally by the CrIS (other than the minor out of band

response), M12 and M14 are located in the spectral gaps of the CrIS data. Since both the VIIRS and CrIS are on the same platform of the Suomi NPP, the collocation is straightforward. AVHRR channels 4 and 5 spectrally match the VIIRS M15 and M16, respectively. MODIS band B31 and B32 are comparable to the M15 and M16. The VIIRS, MODIS, and AVHRR data are averaged over a grid of a 0.25 by 0.25° in the validation study. Data are selected when the standard deviation of the brightness temperature in each grid is less than 0.6 K.

[35] VIIRS M15 and AVHRR channel 4, as well as the VIIRS M16 for AVHRR channel 5 agree well in brightness temperature. Early comparison between AVHRR ch 4 and 5, and VIIRS M15 and M16 for a selected data (13:45 UTC on 4 March 2012) shows that the two data sets agree with a standard deviation of 0.2 K and a mean bias of 0.3 K. The main cause for the bias is due to the small difference in spectral responses of the two sensors and view zenith angles. To account for this effect, the Community Radiative Transfer Model (CRTM) and the European Centre for Medium-Range Weather Forecast (ECMWF) analysis data are used to simulate the VIIRS and AVHRR radiances with the specific view geometry. Using a double difference technique, it was found that the bias between the AVHRR and the VIIRS is on the order of 0.1 K after the spectral differences are accounted for (Figure 6b).

[36] Since both VIIRS and CrIS are on the same satellite and share the same geolocation algorithm, it allows us to precisely collocate measurements from the two sensors. The VIIRS data are averaged spatially to match the CrIS pixel size and convolved spectrally to match the VIIRS RSR. Results show that both CrIS and VIIRS for M15 and 16 agree well generally. However, a more detailed VIIRS and CrIS comparison showed a scene temperature dependent bias (VIIRS M15 − CrIS = −0.4 K) at a low scene temperature of 200 K [*Tobin et al.*, 2013], which is currently being investigated.

[37] The VIIRS data users reported that the M12 image has striping during daytime at high scan angles. The striping in the along-track direction displays a periodic pattern due to the fact that VIIRS uses 16 detectors for each M band and 32 detectors for each I band. Since the striping is not
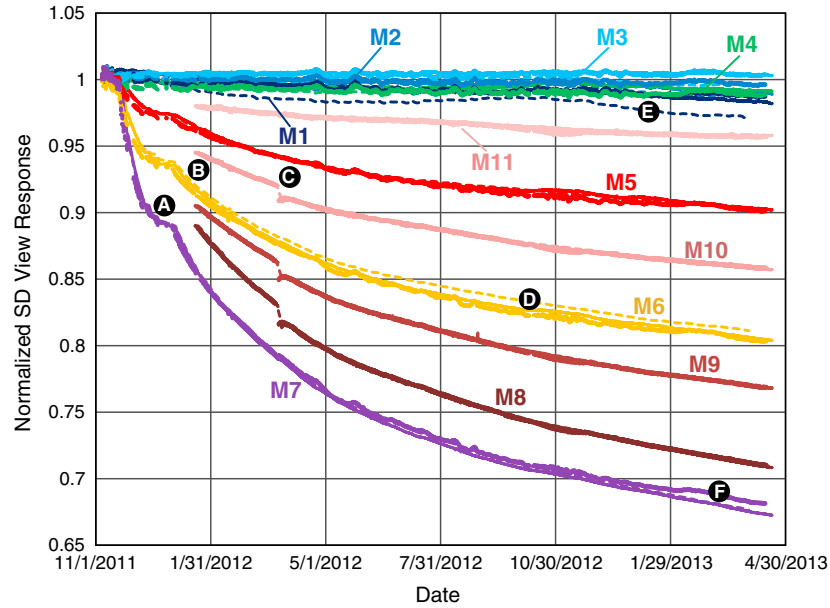
(a). Comparison of the VIIRS F-Factor trending (IDPS=dashed lines, VCST=solid lines, ICVS=dots)
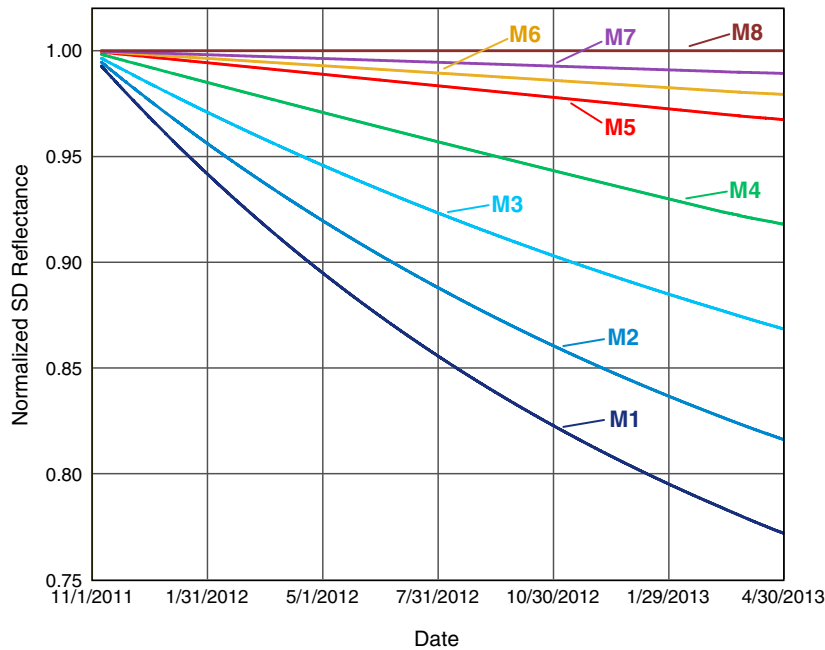
(b). VIIRS Solar Diffuser (SD) degradation

Figure 7. VIIRS Instrument Degradation. (a) Comparison of the VIIRS F factor trending (IDPS = dashed lines, VCST = solid lines, ICVS = dots); (b) solar diffuser degradation.

observed at nighttime, investigation reveals that the striping was largely due to the difference in sensor azimuth angles among the 16 detector [*Liu et al.*, 2013]. Finally, the VIIRS SDR team has been working closely with the Sea Surface Temperature (SST) EDR team to address any VIIRS TEB performance issues. Overall, the team found that the SST bands of VIIRS are of high quality and the SST retrieved from VIIRS observations is in agreement on the order of 0.1 K with established references by the SST community [*Liang and Ignatov*, 2013].

6. Long-Term Monitoring of VIIRS Instrument Performance

[38] An Integrated Calibration/Validation System (ICVS) has been developed over the years [*Cao et al.*, 2006] and now extended to support the calibration and validation of Suomi NPP. A large number of parameters generated or used by the Interface Data Processing Segment (IDPS—the official system for the production of VIIRS SDR) are monitored in near real time for the Suomi NPP spacecraft as well as for
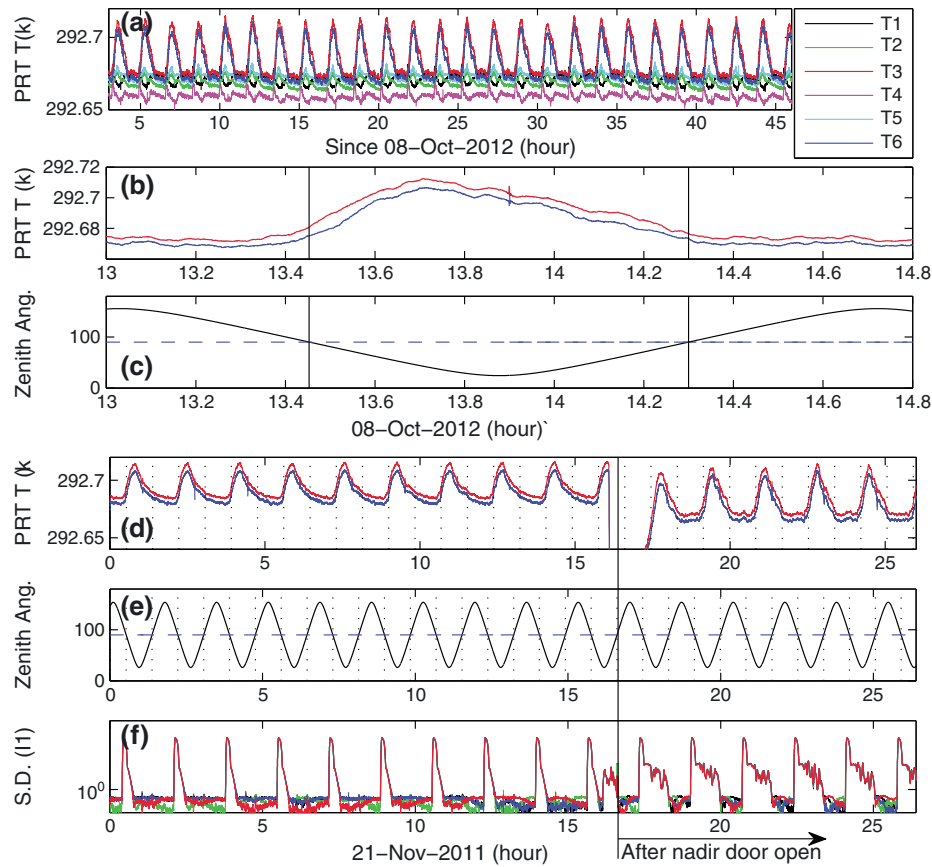
Figure 8. Stability of the VIIRS onboard calibrator: (a) thermistor variations (~ 2 days); (b) and (c) one orbit variation in relation to solar zenith angle for the two anomalous thermistors; (d) and (e) thermistors variation in relation to solar zenith angle before and after nadir door open; (f) I1 solar diffuser view variation before and after nadir door open.

all major instruments. The ICVS also provides continuous tracking of these parameters in various time resolutions such as daily, monthly, and yearly. The monitoring is accessible online through the VIIRS website https://cs.star.nesdis.noaa.gov/NCC/VIIRS.

[39] Long-term trending of the VIIRS instrument performance includes the time series of VIIRS component temperatures, counts for SD, SDSM, space view, OBCBB, F factors for SD and H factor for SDSM, noise, and gain. The instrument performance trending is very useful for anomaly detection. Three specific applications of the monitoring system are discussed below to exemplify its use:

6.1. F Factor Trending and Comparisons

[40] The F factor for the RSB is used to update the calibration coefficients and compensate for the changes in VIIRS optical instrument responsivity, and it directly affects the calibration accuracy of the RSB. The F-LUT has been independently produced by three groups within the VIIRS SDR team (The Aerospace team for the IDPS, the NASA VCST team, and the NOAA ICVS team). The LTM of the VIIRS RSB responsivity degradation seen from SD data and the chronological details have been discussed in *Cao et al.*, 2013a. Figure 7 shows the comparison of the F factor trending produced by the three teams. In addition to events discussed in *Cao et al.*, 2013a (Points A, B, and C), several additional observations can be made. While these three versions in

general agree with each other for all bands, there are detailed differences. For example, for the M7 band, one curve (ICVS) deviated from the other two curves since January 2013 (Point F), likely due to a processing change. For M1 to M3 bands, a good agreement between the NASA and ICVS version is observed, while a deviation on the order of 1% is found for the IDPS version (Point E). The differences for M6 appear to be caused by a normalization issue as to where the first data point was used (Point D). Although the differences are very small, they directly affect the calibration accuracy of these bands and therefore the causes for the differences will be further investigated and corrected as needed. Figure 7b shows that the solar diffuser itself has significant degradation due to exposure to sunlight (lack of SD door) especially in the short wavelength bands, although its effect is calibrated out.

6.2. Blackbody Temperature Orbital Variation

[41] The OBCBB temperature is controlled using heater elements and thermistors of the encapsulated glass-bead type (VIIRS Calibration ATBD), in contrast to the traditional Platinum Resistance Thermometers (PRTs). Figures 8a–8c show the temperature variations of the six blackbody thermistors. Thermistors 1, 2, 4, and 5 have temperature variation within 0.01 K orbitally. However, thermistors 3 and 6 vary between 292.66 K and 292.72 K and have an orbital peak to valley temperature variation of ~0.05K. This behavior reflects nonuniform variations in the effective temperature of

the OBCBB-radiating surface. Analysis of the occurrence of maximum orbital temperature change of thermistors shows that peak thermistor temperature variations occur during Suomi NPP daytime. At night when the sunlight is completely blocked by the Earth, the temperatures of thermistor 3 and 6 are stable at their minimum with small fluctuations due to noise.

[42] Figures 8d and 8e show that the orbital variation existed before the opening of nadir door on 21 November 2011. After the nadir door opening, the amplitudes of the temperature variation for thermistors 3 and 6 are slightly larger. These analyses suggest that the orbital variation of the thermistors 3 and 6 temperatures is mainly due to the nonuniform warming up of the VIIRS instrument when the sunlight illuminates the instrument during the day.

6.3. Earth Contamination of the Solar Diffuser

[43] Figure 8f shows radiometric measurements of VIIRS I1 band when the telescope views the SD. The Space View (SV) background has been subtracted from the measurements. The I1 view of SD shows that before opening of the nadir door, the data appear as one clean spike indicating the time interval when the SD is illuminated by the sunlight when it passes through the SD screen. This occurs when the satellite passes from the dark side to the sunlit side of the Earth in the high latitudes of the southern hemisphere. After the opening of the nadir door, side lobes appeared in the I1 view of SD in addition to the main spike. These variations in the I1 view of SD occur when Suomi NPP is on the dayside and coincide with the variation of the thermistor temperature. This suggests that the side lobes in the I1 view of SD is likely due to the reflected sun light from Earth which enters through the VIIRS nadir door, contaminating the SD and is observed by the I1. Although the impact on calibration appears negligible, further assessment is needed.

7. Lessons Learned and Remaining Issues

[44] The work of the VIIRS SDR team with seven major organizations greatly contributed to the high quality of the VIIRS SDR data. The team consists of world class experts with considerable experiences in performing in-depth studies of many technical issues. For example, multiple tests of the VIIRS relative spectral response (RSR) were performed and the data were analyzed for out-of-band response down to the 10^{-7} level on a scale from 0.0 to 1.0, compared to the traditional 10^{-1} level of analysis (e.g., AVHRR). However, the multiorganizational team also brings some challenges because several versions of the RSR have been created by different organizations which also lead to discrepancies (for which a discrepancy report system is available in the program) and in turn may cause differences in derived products. Although the vendor version of the RSR is implemented in the operations, a government "best effort" version is also published online, despite the negligible impacts between versions for most applications. In addition, in response to the RTA mirror degradation, a degradation modulated RSR based on the vendor version was also created and implemented in the operations as of 5 April 2013. The difference between the initial and modulated versions of the RSR can lead to radiance biases on the order of 0.2% for M1 and M4 (impact on M1

primarily due to its out-of-band response), and further updates to the modulated RSR will be evaluated in the future.

[45] The VIIRS calibration lookup tables (LUTs) should have been better tested and, if needed, promptly corrected before the launch of the satellite. Some of the VIIRS SDR LUTs prepared before launch were found to be incorrect and required update, such as LUTs for the instrument alignment relative to the spacecraft which affected geographic locations and calculations of solar illumination on the SD. The thermistor coefficients for the OBCBB were also found incorrect in the initial checkout. An incorrect version of the solar irradiance LUT was also identified. Instead of the *Thuillier et al.* 2003 version as the team had assumed (Table 2), a version from the MODTRAN was used in the operations. This can cause discrepancies and biases in several RSB when comparing radiances as shown for the Esun values in Table 2 (~2% for M2, M10, M11, and I3), with smaller impacts on reflectance based comparisons. Ideally, this should be corrected in the operations; however, a sudden change in the solar irradiance values would cause a number of discrepancies and may affect the VIIRS EDR algorithms as well. Also, a large amount of VIIRS SDR data had already been produced when this was found. Nevertheless, users should be aware of this issue especially in radiance comparisons which can be off by more than 2% due to the solar irradiance differences (see Table 2), and it should be resolved in the future.

[46] Another lesson learned is that absolute radiometric accuracy for satellite radiometers is difficult to achieve and validate. Assumptions of "well-calibrated" sensors may not be valid at all times and under different conditions, as in the case of MODIS B8, which could have up to 5% bias (scan angle dependent) in the late part of its collection 5, compared to well accepted MODIS calibration accuracy of 2% in reflectance. This also highlights the challenges in achieving and maintaining the absolute calibration accuracy for satellite radiometers, especially in the reflective solar spectra, since currently there is no absolute radiometric standard on orbit.

[47] Although significant progress has been made in resolving a large number of issues with VIIRS SDR, several issues still need to be fully resolved or closely monitored: (1) The VIIRS scan looses sync from time to time and needs to be closely monitored. The first sync loss occurred a few days after the nadir door was opened in 2011, while the latest event occurred on 7 June 2013. Data are typically lost during sync loss, which lasts on the order of minutes. (2) The VIIRS RTA degradation needs to be closely monitored and its effects accounted for in the data processing to ensure the SDR quality over the mission life. (3) An automated calibration algorithm (K. Rausch et al., Automated calibration of the Suomi NPP VIIRS reflective solar bands, submitted to *Journal of Geophysical Research: Atmospheres*, 2013) will be implemented in the operations in 2013. Although this algorithm has been peer reviewed, a longer time period is needed to evaluate the algorithm performance after its implementation in the operations. (4) The VIIRS DNB stray light near the terminator is causing significant artifacts in the DNB images. While the root cause at the instrument level has yet to be determined, an empirical correction algorithm has been developed by the VIIRS SDR team and will be implemented in 2013. Since this problem has a seasonal cycle with the changing relative position of the sun, the performance of the correction algorithm needs to be thoroughly

evaluated over a period of at least 1 year. (5) Striping is a concern for areas with great scene uniformity and requires further investigation. (6) Reprocessing of the VIIRS SDR data is desirable for time series analysis partly due to numerous corrections since launch but is not in the current base line of the program. (7) Radiometric intercomparisons between CrIS and VIIRS on the Suomi NPP suggest that a bias on the order of 0.4 K exists at cold scene around 200 K. While several hypotheses have been formulated for both VIIRS and CrIS, investigation is still ongoing to find the root cause of the bias.

[48] It is noted that several issues documented previously [*Cao et al.*, 2013a] have been resolved. For example, the effect of switching the scan controller electronics from the B side to the A side on geolocation has been investigated, which led to the updated geolocation lookup table on 11 December 2012 (Wolfe et al., personal communications, 2012]. The M6 saturation issue has been partially resolved after a flag was implemented in October 2012, after which the highest out-of-range radiance value in the M6 SDR is 60 $W \cdot m^{-2} \cdot sr^{-1} \cdot \mu m^{-1}$. The RTA degradation has also alleviated saturation for this band as noted earlier. The gain mixing issue for the dual-gain bands was corrected and validated on 2 April 2012 for M13 (I. Csiszar et al., Active fires from the Suomi NPP visible/infrared/imager/radiometer suite: Product status and first evaluation results, submitted to *Journal of Geophysical Research: Atmospheres*, 2013), and 15 October 2012 for the RSB (Wei, personal communications, 2012).

8. Conclusions

[49] VIIRS represents a new era of moderate-resolution imaging capabilities following the legacy AVHRR and MODIS. The VIIRS instrument on Suomi NPP has been working very well since launch after a number of issues are resolved through postlaunch verification and validation, and the data have achieved provisional maturity status. The radiometric uncertainty for the RSB is generally believed to be comparable to that of MODIS within 2% in reflectance, while an agreement on the order of 0.1 K with AVHRR and other existing references for the sea surface temperature bands has been reached. Accurate VIIRS SDR data are highly desirable for the large number of applications in the areas of land, ocean, and atmosphere, and the data users are generally satisfied with the data quality, although incremental improvements are expected in the near future. The unexpected fast degradation in the rotating telescope assembly mirrors is gradually leveling off but still needs to be closely monitored. The lessons learned in the postlaunch Cal/Val process will be valuable for the future Joint Polar Satellite System (JPSS) mission. The VIIRS SDR team will continue the Cal/Val and long-term monitoring to ensure the data quality of the VIIRS SDR for all applications.

References

Blonski, S., C. Cao, S. Uprety, and X. Shao (2012), Using Antarctic Dome C site and simultaneous nadir overpass observations for monitoring radiometric performance of NPP VIIRS instrument, Geooscience and Remote Sensing Symposium (IGARSS).

Cao, C., and A. Heidinger (2002), Inter-comparison of the longwave infrared channels of MODIS and AVHRR/NOAA-16 using simultaneous nadir observations at orbit intersections, Earth Observing Systems VII, Proceedings of SPIE, Vol. 4814.

Cao, C., M. Weinreb, and H. Xu (2004), Predicting simultaneous nadir overpasses among polar-orbiting meteorological satellites for the intersatellite calibration of radiometers, *J. Atmos. Oceanic Technol.*, 21, 537–542.

Cao, C., F. Weng, M. Goldberg, X. Wu, and J. Sullivan (2006), Toward an integrated system for the calibration/validation of multisensor radiances from operational satellites, American Meteorological Society Annual Meeting Proceeding, Available at https://ams.confex.com/ams/pdfpapers/99732.pdf.

Cao, C., S. Uprety, J. Xiong, A. Wu, P. Jing, D. Smith, G. Chander, N. Fox, and S. Ungar (2010), Establishing the Antarctic Dome C community reference standard site towards consistent measurements from Earth observation satellites, *Can. J. Remote Sens.*, 36(5), 498–513, doi:10.5589/m10-075.

Cao, C., F. Deluccia, X. Xiong, R. Wolfe, and F. Weng (2013a), Early on-orbit performance of the Visible Infrared Imaging Radiometer Suite (VIIRS) onboard the Suomi National Polar-Orbiting Partnership (Suomi-NPP) satellite, *IEEE Trans. Geosci. Remote Sens.*, doi:10.1109/TGRS.2013.2247768.

Cao, C., X. Shao, S. Uprety (2013b), Detecting light outages after severe storms using the Suomi-NPP/VIIRS day/night band radiances, *IEEE Geosci. Remote Sens. Lett.*, doi:10.1109/LGRS.2013.2262258.

Chand, T. R. K., K. V. S. Badarinath, C. D. Elvidge, and B. T. Tuttle (2009), Spatial characterization of electrical power consumption patterns over India using temporal DMSP-OLS night-time satellite data, *Int. J. Remote Sens.*, 30(3), 647–661.

Deluccia, F., D. I. Moyer, E. H. Johnson, K. W. Rausch, N. Lei, K. Chiang, and X. Xiong (2012), Discovery and characterization of on-orbit degradation of the VIIRS rotating telescope assembly, Proc. SPIE, vol. 8510, p. 85101A, Oct. 2012.

Doll, C. N. H., J.-P. Muller, and J. G. Morley (2006), Mapping regional economic activity from night-time light satellite imagery, *Ecol. Econ.*, 57(2006), 75–92.

Fuqua, P. D., J. D. Barrie, M. J. Meshishnek, M. Ciofalo, C. Chu, J. Chaney, R. Moision, and L. Graziani (2012), Root cause determination of on-orbit degradation of the VIIRS rotating telescope assembly, Proc. SPIE, vol. 8510.

Guenther, B., X. Xiong, V. V. Salomonson, W. L. Barnes, and J. Young (2002), On-orbit performance of the Earth observing system moderate resolution imaging spectroradiometer; first year of data, *Remote Sens. Environ.*, 83, 16–30.

Heidinger, A. K., C. Cao, and J. T. Sullivan (2002), Using Moderate Resolution Imaging Spectrometer (MODIS) to calibrate advanced very high resolution radiometer reflectance channels, *J. Geophys. Res.*, 107(D23), 4702, doi:10.1029/2001JD002035.

Hutchinson, K. D., and A. P. Cracknell (2006), *Visible Infrared Imager Radiometer Suite—A New Operational Cloud Imager*, pp. 230, Taylor & Francis, New York, USA.

Iona, G., et al. (2012), VIIRS on-orbit optical anomaly: Lessons learned, Proc. SPIE, vol. 8510, p. 85101C, Oct. 2012.

Johnston, A. H. (2000), Radiation damage of electronic and optoelectronic devices in space, in Proc. 4th Int. Workshop Radiat. Effects Semicond. Devices Space Appl., Oct. 2000.

JPSS (2013), Joint Polar Satellite System (JPSS) Program Level 1 Requirements, Version 2.7, January 30, 2013, pp.151.

Lee, T., S. Miller, C. Schueler, and S. Miller (2006), NASA MODIS previews NPOESS VIIRS capabilities, *Weather Forecast.*, 21(4), 649–655.

Liang, X., and A. Ignatov (2013), AVHRR, MODIS, and VIIRS radiometric stability and consistency in SST bands, *J. Geophys. Res., Atmos.*, 118, 3161–3171, doi:10.1002/jgrc.20205.

Liu, Q., C. Cao, and F. Weng (2013), Assessment of Suomi National Polar-Orbiting Partnership VIIRS emissive band calibration and inter-sensor comparisons, *IEEE J. Sel. Topics Appl. Earth Observ.*, doi:10.1109/JSTARS.2013.2263197.

Loeb, N. G. (1997), In-flight calibration of NOAA AVHRR visible and near-IR bands over Greenland and Antarctica, *Int. J. Remote Sens.*, 18(3), 477–490.

Miller, S. D., and R. E. Turner (2009), A dynamic lunar spectral irradiance data set for NPOESS/VIIRS day/night band nighttime environmental applications, *IEEE Trans. Geosci. Remote Sens.*, 47, 2316–2329.

Miller, S. D., S. P. Mills, C. D. Elvidge, D. T. Lindsey, T. F. Lee, and J. D. Hawkins (2012), Suomi satellite brings to light a unique frontier of nighttime environmental sensing capabilities, *Proc. Natl. Acad. Sci. U.S.A.*, *109*(39), 15,706–15,711.

Murgai, V., N. R. Nelson, E. H. Johnson, and K. E. Yokoyama (2012), VIIRS VisNIR/SMWIR end-of-life sensitivity predictions, Proceedings of SPIE, Earth Observing Systems, 2012.

Murphy, R. P., P. E. Ardanuy, F. Deluccia, J. E. Clement, and C. Schueler (2006), The visible infrared imaging radiometer suite, in *Earth Science Satellite Remote Sensing*, vol. 1, pp. 199–223, Springer-Verlag, New York, USA.

Shang, Z., M. Jiang, and M. Pu (2008), Laver cultivation and climate suitability analysis of Jiangsu province, *J. Agr. Sci.*, *36*(13), 5315–5319.

Six, D., M. Fily, S. Alvain, P. Henry, and J.-P. Benoist (2004), Surface characterisation of the Dome Concordia area (Antarctica) as a potential satellite calibration site, using Spot 4/Vegetation instrument, *Remote Sens. Environ.*, *89*, 83–94.

Tobin, D., et al. (2013), Suomi NPP/JPSS Cross-Track Infrared Sounder (CrIS): Intercalibration with AIRS, IASI, and VIIRS, Ams Annual Conference.

Thuillier, G., M. Hersé, D. Labs, T. Foujols, W. Peetermans, D. Gillotay, P. C. Simon, and H. Mandel (2003), The solar spectral irradiance from 200 to 2400 NM as measured by the SOLSPEC spectrometer from the ATLAS and EURECA missions, *Sol. Phys.*, *214*, 1–22.

Uprety, S., and C. Cao (2012), Radiometric and spectral characterization and comparison of the Antarctic Dome C and Sonoran Desert sites for the calibration and validation of visible and near-infrared radiometers, *J. Appl. Remote Sens.*, *6*(1), 063541, doi:10.1117/1.JRS.6.063541.

Wolfe, R., G. Lin, M. Nishihama, K. P. Tewari, and E. Montano (2012), NPP VIIRS early on-orbit geometric performance, Proc. SPIE, Vol. 8510, P.851013, Oct. 2012.

Xiong, X., et al. (2013), VIIRS on-orbit calibration methodology and performance, *J. Geophys. Res. Atmos.*, doi:10.1002/2013JD020423.

Zhuo, L., T. Ichinose, J. Zheng, J. Chen, P. J. Shi, and X. Li (2009), Modeling the population density of China at the pixel level based on DMSP/OLS non-radiance-calibrated night-time light images, *Int. J. Remote Sens.*, *30*(4), 1003–1018.